TOP 5 E-POSTER PRESENTATIONS

Artificial Intelligence in Pediatric Intussusception Detection: A Systematic Review and Meta-analysis

Jessica Christanti[1], Ratna Sutanto[1,2], Jeanne Leman[1,2]

[1] Radiology Department, Medical Faculty of Pelita Harapan University, Indonesia
[2] Radiology Department, Siloam Hospitals Lippo Village, Jakarta, Indonesia

UPH UNIVERSITAS PELITA HARAPAN

ARTIFICIAL INTELLIGENCE IN PEDIATRIC INTUSSUSCEPTION DETECTION: A SYSTEMATIC REVIEW AND META-ANALYSIS

Siloam Hospitals

Jessica Christanti[1], Ratna Sutanto[1,2], Jeanne Leman[1,2]
[1] Radiology Department, Medical Faculty of Pelita Harapan University, Indonesia
[2] Radiology Department, Siloam Hospitals Lippo Village, Jakarta, Indonesia

BACKGROUND & PURPOSE

Intussusception needs to be diagnosed immediately to prevent complications such as ischemia and intestinal perforation. It can be diagnosed by a colon in the loop, abdominal radiograph, and ultrasound, with the best accuracy on ultrasound. Artificial intelligence (AI) is expected to help radiologists and clinicians make the diagnosis.

This systematic review and meta-analysis will assess the diagnostic accuracy of AI-based radiology modalities in pediatric intussusception.

METHODS

- 8 Databases dan 1 Registry: Pubmed, Scopus, Proquest, MedRxiv, BioRxiv, SSRN, Cochrane Central, Google Scholar, and PROSPERO until June 8, 2024.
- This study already registered in PROSPERO (ID: 543569)
- The diagnostic value of AI-based radiology modalities : pooled sensitivity, specificity, positive likelihood ratio (PLR), negative likelihood ratio (NLR), diagnostic odds ratio (DOR), and area under the curve (AUC).
- Meta-analyses were performed using STATA 17.0 (Stata Corp LP, TX, USA), and Meta-DiSc 2.0 (Romany Cajal Hospital, Madrid, Spain)
- QUADAS 2 to assess the risk of bias and APPRAISE-AI to evaluate the quality of AI studies.
- Heterogeneity analysis was performed using receiver operating characteristic (ROC) and sensitivity analysis.
- The clinical utility of AI-based radiology modalities was assessed using Fagan's nomogram.

INCLUSION

- Diagnostic study design,
- Studies that include AI assessment for Intussusception,
- Human-based studies,
- Absolute numbers of true-positive, false-positive, or false negative, or true-negative could be calculated from the study.

EXCLUSION

- Non-human subject research,
- Case report/series
- Commentary/viewpoint,
- Narrative review,
- Irretrievable full-text article.

RESULT

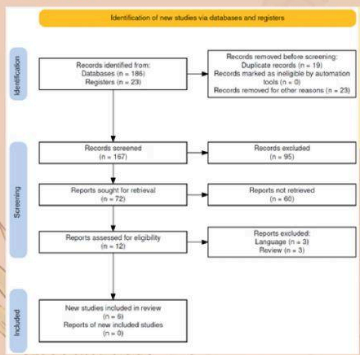

Figure 1. Preferred Reporting Items for Systematic Reviews and Meta-Analyses (PRISMA) 2020 flow chart of the study selection process

Author	Year	Imaging Modality	No. images per set			Reference Standard	TN	FP	FN	TP	Algorithm
			Training	Tuning	Testing						
Kwon et al.	2020	Abdominal Radiography	11384	11384	255	Expert consensus	4633	349	130	594	Deep convolutional neural network (CNN)
Kim et al.	2019	Abdominal Radiography	681	NR	75	Expert consensus	48	2	6	19	The You-Only-Look-Once (YOLO)v3
Xiong Chen et al.	2023	Ultrasound	6959	1927	985	Expert consensus	798	33	532	2791	Children Intussusception Diagnosis Network (CIDNet)
Zheming Li et al.	2022	Ultrasound	2325	586	142	Expert consensus	411	35	7	133	Region Convolutional Neural Network features (RCNN)
Kim et al.	2023	Ultrasound	38148	5724	2617	Expert consensus	103	1	0	20	The YOLOv5 Architecture
Pei et al.	2023	Ultrasound	6081	2023	632	Expert consensus	182	6	12	227	Modified YOLOv5

TN: True Negative, FP: False Positive, FN: False Negative, TP: True Positive
Table 1. Characteristics of AI Studies on Pediatric Intussusception

	Estimate	95% LCI	95% UCI
Sensitivity	0.901	0.823	0.947
Specificity	0.953	0.928	0.969
DOR	183.778	81.815	412.814
LR+	19.023	12.353	29.295
LR-	0.104	0.056	0.19

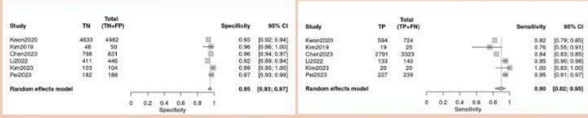

Figure 2. Forest plot of diagnostic value for Artificial Intelligence in detecting Pediatric Intussusception.

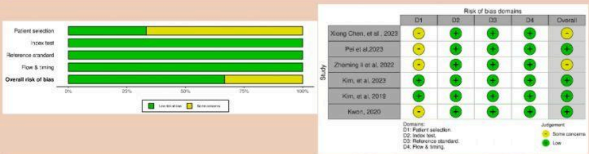

Figure 3. Quality Assessment of Included Study

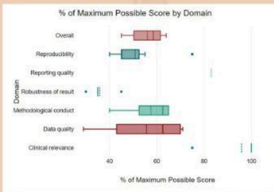

Figure 4. APPRAISE-AI Domain and Overall Scores

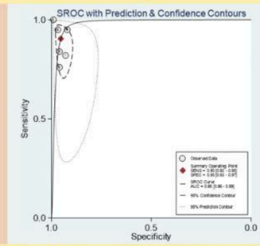

Figure 5. Summary Receiver Operating Characteristics (SROC) curve of Artificial Intelligence in detecting Pediatric Intussusception

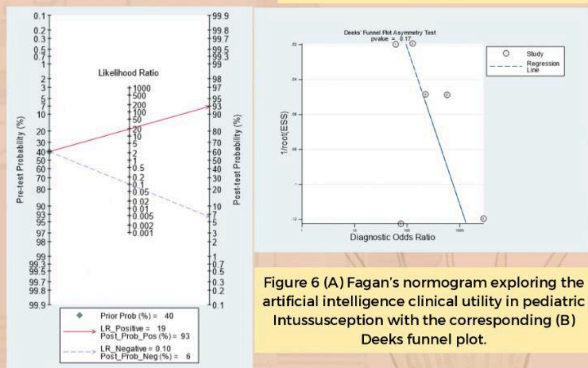

Figure 6 (A) Fagan's normogram exploring the artificial intelligence clinical utility in pediatric Intussusception with the corresponding (B) Deeks funnel plot.

CONCLUSION

AI-based ultrasound and abdominal radiograph modalities can help clinicians identify Intussusception. Korea and China are suitable populations for implementation.

REFERENCES

1. Kim S, Yoon H, Lee MJ, et al. Performance of deep learning-based algorithm for detection of ileocolic intussusception on abdominal radiographs of young children. Sci Rep; 9. Epub ahead of print 1 December 2019. DOI: 10.1038/s41598-019-55536-6.
2. Pei Y, Wang G, Cao H, et al. A deep-learning pipeline to diagnose pediatric intussusception and assess severity during ultrasound scanning: a multicenter retrospective-prospective study. NPJ Digit Med; 6. Epub ahead of print 1 December 2023. DOI: 10.1038/s41746-023-00930-8.
3. Kwong JCC, Khondker A, Lajkosz K, et al. APPRAISE-AI Tool for Quantitative Evaluation of AI Studies for Clinical Decision Support. JAMA Netw Open. Epub ahead of print 2023. DOI: 10.1001/jamanetworkopen.2023.35377.
4. Wiyarta E, Nugraha DA, Ramadani MI, et al. Clinical utility and diagnostic value of tumor-educated platelets in lung cancer: a systematic review and meta-analysis. Frontiers in Oncology; 13. Epub ahead of print 2023. DOI: 10.3389/fonc.2023.1201713.
5. Chen X, You G, Chen Q, et al. Development and evaluation of an artificial intelligence system for children intussusception diagnosis using ultrasound images. iScience; 26. Epub ahead of print 21 April 2023. DOI: 10.1016/j.isci.2023.106456.
6. Li Z, Song C, Huang J, et al. Performance of Deep Learning-Based Algorithm for Detection of Pediatric Intussusception on Abdominal Ultrasound Images. Gastroenterol Res Pract; 2022. Epub ahead of print 2022. DOI: 10.1155/2022/9285238.
7. Kwon G, Ryu J, Oh J, et al. Deep learning algorithms for detecting and visualising intussusception on plain abdominal radiography in children: a retrospective multicenter study. Sci Rep; 10. Epub ahead of print 1 December 2020. DOI: 10.1038/s41598-020-74653-1.
8. Kim SW, Cheon JE, Choi YH, et al. Feasibility of a deep learning artificial intelligence model for the diagnosis of pediatric ileocolic intussusception with grayscale ultrasonography. Ultrasonography 2024; 43: 57-67.

High-pitch Photon-counting CT of the Trunk for Small Children

Tetsu Niwa

Department of Diagnostic Radiology, Tokai University School of Medicine

High-pitch photon-counting CT of the trunk for small children

Tetsu Niwa, MD, PhD, **Department of Diagnostic Radiology, Tokai University School of Medicine**

Background: Recently introduced photon-counting computed tomography (CT) features a new detector system, which directly convert X-ray photons to electrical signals, thereby providing high image quality. The clinically available photon-counting CT has dual-source systems that enable rapid scanning, which could be beneficial for scanning small children to reduce motion artifacts. However, image quality of high-pitch PCCT for small children is not well understood.

Purpose: The aim of this study was to assess the image quality of PCCT using high-pitch image acquisition for the trunk of small children.

Methods: PCCT images obtained with high-pitch image acquisition for 54 children under 5 years old were retrospectively assessed. CT images with a thickness of 1 mm were evaluated in terms of visibility of the lung, abdominal major organs, and great vessels, artifact, noise, and overall image quality were rated by a broad-certified radiologist on a 5-point scale (1=non-diagnostic; 5=excellent). The visibility of the grate vessels was only assessed on contrast-enhanced CT. Volume CT dose index (CTDIvol) of each CT examination was recorded.

Results: This study included 20 non-contrast CT and 34 contrast-enhanced CT examinations. Mean pitch used was 2.4 (range, 2.0–3.0). Mean score (range) for visibility of the lung and abdominal organs, great vessels, artifact, and noise were 4.6 (3–5), 4.1 (3–5), 4.5 (4–5), 4.4 (3–5), and 4.1 (3–5), respectively. Mean score (range) for overall image quality was 4.3 (3–5). Mean CTDIvol was 1.71 ± 0.22 mGy.

Conclusion: High-pitch PCCT generally provides good image quality for the trunk of small children.

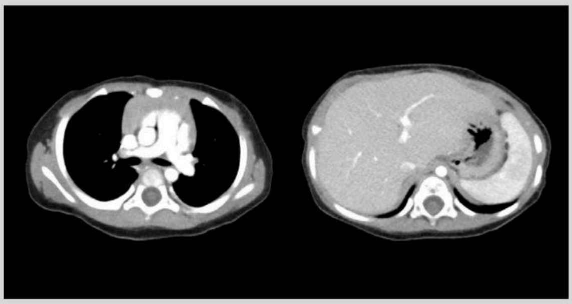

9-month-old, inspiratory stridor
BW 7.3 kg
Pitch = 2.7
Acquisition time ≒ 0.5 s
CTDIvol 1.9 mGy

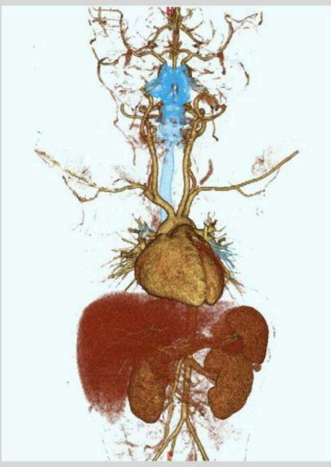

References

1. Flohr T, et al. Photon-counting CT review. Phys Med. 2020;79:126-36.

2. Leng S, et al. Photon-counting detector CT: system design and clinical applications of an emerging technology. Radiographics. 2019;39(3):729-43.

MR Features in Advanced Retinoblastoma - What a Paediatric Radiologist Needs to Know

L Ching[1], KFK Fung[2], ES Wong[3], JC Yam[3], YLE Kan[2]

[1] Department of Diagnostic and Interventional Radiology, Queen Elizabeth Hospital, Hong Kong SAR
[2] Department of Radiology, Hong Kong Children's Hospital, Hong Kong SAR
[3] Department of Ophthalmology and Visual Sciences, Chinese University of Hong Kong, Hong Kong SAR

MR Features in Advanced Retinoblastoma – What a Paediatric Radiologist Needs to Know

L Ching[1], KFK Fung[2], ES Wong[3], JC Yam[3], YLE Kan[2]
[1]Department of Diagnostic and Interventional Radiology, Queen Elizabeth Hospital, Hong Kong SAR
[2]Department of Radiology, Hong Kong Children's Hospital, Hong Kong SAR
[3]Department of Ophthalmology and Visual Sciences, Chinese University of Hong Kong, Hong Kong SAR

伊利沙伯醫院 QUEEN ELIZABETH HOSPITAL

香港兒童醫院 Hong Kong Children's Hospital

Introduction

- Retinoblastoma is the most common intra-ocular malignancy in children worldwide, with an estimated incidence of 1 per 18,000-30,000 live births.
- Precise identification of these features and accurate staging are important for oncologists and interventional radiologists to formulate the treatment plan and estimate the prognosis for parental counselling.

Retinoblastoma Staging

- According to the current retinoblastoma staging systems, there are multiple features indicating advanced disease.
- Current treatment modalities include focal therapy such as laser or cryotherapy, intravenous chemo-therapy, intra-arterial chemotherapy and surgical enucleation. Focal therapy is proven to be effective only in relatively early stage disease.
- For advanced stage disease, surgical enucleation, neoadjuvant and adjuvant systemic chemotherapy are recommended to reduce the recurrence rate and improve the overall survival.
- However, surgical enucleation is well known to impose significant side effect on patient's daily life, in particular permanent loss of vision in one eye.
- Therefore, accurate staging, in particular correctly recognizing the features indicative of high grade disease, is essential to avoid unnecessary or delay the indicated vision-losing surgery and adjuvant therapy.

AJCC Clinical Staging 8th edition, 2017	ICRB group Shields, 2006	Recommended treatment
cT1 Intra-retinal tumour(s) with subretinal fluid ≤5 mm from base of any tumour cT1a Tumours ≤3 mm and further than 1.5 mm from disc and fovea cT1b Tumours >3 mm or closer than 1.5 mm from disc or fovea	 A, > 3mm to fovea or B, 1.5 to 3 mm B, ≤3 mm or C, 3 to 5 mm	For ICRB group A or B: • laser coagulation • Thermtherapy • Cryotherapy • Brachytherapy
cT2 Intraocular tumour(s) with retinal detachment, vitreous seeding, or subretinal seeding. cT2a Subretinal fluid >5 mm from the base of any tumour cT2b Vitreous seeding and/or subretinal seeding	 C, or E, tumour >50% of eye volume C, ≤3 mm or D, > 3 mm or E, tumour >50% of eye volume	For ICRB group C: • Systemtic chemotherapy • Intra-arterial chemotherapy • Intra-vitreal chemotherapy
cT3 Advanced intraocular tumour(s) cT3a Phthisis or pre-phthisis bulbi cT3b Tumour invasion of choroid, pars plana, ciliary body, lens, zonules, iris, or anterior chamber cT3c Raised intraocular pressure with neovascularization and/or buphthalmos cT3d Hyphaema and/or massive vitreous haemorrhage cT3e Aseptic orbital cellulitis	 E E E E E	For ICRB group D or E: • Systemtic chemotherapy • Intra-arterial chemotherapy • Intra-vitreal chemotherapy • Enucleation • Adjuvant systemic chemotherapy in selected high risk cases
cT4 Extraocular tumour(s) involving orbit, including optic nerve cT4a Radiologic evidence of retrobulbar optic nerve involvement or thickening of optic nerve or involvement of orbital tissues cT4b Extraocular tumour clinically evident with proptosis and/or an orbital mass		

Table 1: the American Joint Committee on Cancer (AJCC) Clinical Staging 8th edition and the International Classification for Intraocular Retinoblastoma (ICRB) and the recommended treatment

Retinal Detachment

- Under MRI, retinal detachment is characterised by T2-weighted hypointense line which limited anteriorly by the ora serrata, and posteriorly converge on the optic disc

Figure 1: The axial (left) and sagittal (right) MRI T1-weighted images of a 23-month-old boy having retinoblastoma in both eyes. In left eye, there is T1-weighted hypointense retinoblastoma, with adjacent V-shaped T1-weighted hyperintense subretinal tissue converging to the optic disc (white arrow), which is signature for retinal detachment.

Vitreous and subretinal seeding

- Charactertised by small foci of signal that is similar as the primary tumour in the background of the T2 hyperintense vitreous or along the retina.
- Gold standard of detecting seeding is by fundus photography, and the absence of seeding at MRI cannot exclude the presence of seeding due to the small size.

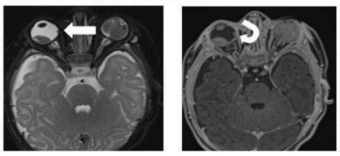

Figure 2 (left) Axial T2-weighted MRI image and (right) axial T1-weighted post-contrast image of a 2-month-old girl with retinoblastoma in both eyes. There is a T2 hypointense focus (arrow) with contrast enhancement (curved arrow) on the medial aspect of right retina, which is suggestive of subretinal seeding.

Choroid invasion

- The choroid is a highly vascular layer underneath and supports the metabolism of retina, and this predisposes the patient to distal metastasis and all-call mortality when it is invaded.
- Traditionally, enucleation of the globe is recommended for retinoblastoma patient with choroid invasion, but recently more and more case reports have shown the success of systemic and intra-arterial chemotherapy in disease control.
- Massive choroidal invasion more than 3mm in post enucleation histopathology indicates high risk disease and warrants the use of adjuvant chemotherapy to reduce the risk of metastasis.
- At MRI, choroid invasion is shown by the discontinuation of the enhancing choroid layer.

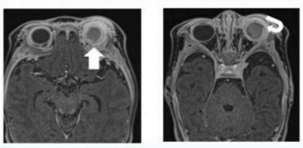

Figure 3 Axial T1-weighted post-contrast MRI images of a 40-day-old girl with left eye retinoblastoma. There is mural defect in the posterior aspect (arrow) and lateral aspect (curved arrow) of the choroid layer of left globe, suggestive of invasion. Noted there is also aseptic orbital cellulitis in the left globe, which is another imaging feature indication of high grade retinoblastoma.

Anterior segment invasion and increase intra-ocular pressure

- Together with increased inflammation in the anterior chamber and direct reduction of its volume, it is common to have elevated intra-ocular pressure at the same time.
- Under MRI, anterior segment invasion is shown by loss of normal plane between the tumour and the anterior chamber structure, in particular the lens and the ciliary body.
- Increase in intra-ocular pressure has to be suspected when there is increase in globe size or reduction of anterior chamber depth

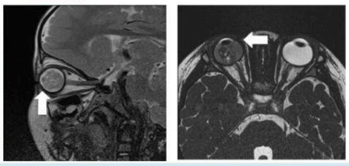

Figure 4 (left) Oblique sagittal T2-weighted MRI image and (right) axial T2-weighted MRI image of a 19-month-old patient with right eye retinoblastoma. The large tumour in posterior aspect of right globe is inseparable with the ciliary body and lens of right eye (arrow), indicative of anterior chamber invasion. The anterior chamber depth of right eye is reduced, which is suggestive of underlying raised intraocular pressure.

Iris neovascularisation

- It is hypothesized that the increase in vascularity can reduce drainage by the lymphatic system secondary to the mass effect of retinoblastoma, promoting the vascular endothelial growth factor release.
- The leaky new vessels allow contrast leakage, shown by increased enhancement in the anterior chamber

Figure 5 (left) Axial image of T1-weighted post contrast MRI image. (right) Oblique sagittal T1-weighted post-contrast MRI image of the left eye of a 13-month-old boy with retinoblastoma. Increase in contrast enhancement of the anterior chamber is seen in left eye when comparing with the normal right eye (arrow).

Vitreous Hemorrhage

- Characterised by diffuse T1-weighted hyperintense which does not drop in signal in fat saturated sequence and T2-weighted hypointense signal in vitreous humour.

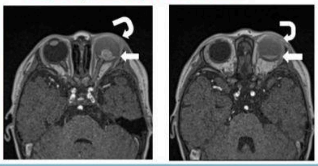

Figure 6 (left) and (right) Axial T1-weighted MRI images of a 13-month-old boy with retinoblastoma of left eye. There is a T1-weighted hyperintense layer (arrow) in the dependent region of vitreous humour of left eye, with diffuse increase in T1-weighted hyperintense signal in rest of its vitreous humour (curved arrow) when comparing with contralateral eye. Features are suggestive of vitreous hemorrhage.

Aseptic orbital cellulitis and lens dislocation

- Retinoblastoma can promote inflammation of the globe leading to aseptic orbital cellulitis
- Under MRI, this is characterized by periocular T2-weighted hyperintense signal with contrast enhancement.
- Lens subluxation is seen often at the same time secondary to ciliary body necrosis.

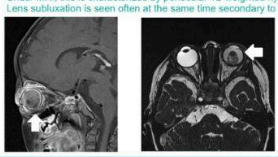

Figure 7 (left) Oblique sagittal T1-weighted post contrast MRI image and (right) axial T2-weighted MRI image of a 13-month-old boy with left eye retinoblastoma. There is increase enhancement in periorbital soft tissue in left eye involving posterior to the orbital septum (arrow), suggestive of orbital cellulitis. There is also posterior subluxation of left lens shown in the T2-weighted image (arrow).

Post-laminar optic nerve invasion

- Presence of optic nerve invasion posterior to lamina cribrosa is a contraindication to intra-arterial chemotherapy and the segmented involved should be included for the enucleation to archive disease-free margin.
- Under MRI, the caliber of the involved optic nerve can be normal, while there can be abnormal enhancement or signal in the post-laminar segment to suggest involvement.

Figure 8 (left) Oblique sagittal T1-weighted post contrast MRI image (right) Axial T2-weighted MRI image of a 14-month-old boy with right eye retinoblastoma. There is subtle increase in contrast enhancement (arrow) and T2-weighted hyperintense signal (curved arrow) in the post-laminar segment of right optic nerve, suggestive of involvement by tumour.

Distant and systemic metastases

- The common sites include the lungs, liver, and marrow.
- Whole body imaging, including CT, MRI, scintigraphy or PET are helpful in evaluation the metastases.

Figure 9 (left) Coronal right knee radiograph and (right) coronal T2-weighted MRI image of a 10-year-old boy with surgical enucleation done bilateral retinoblastoma when he was 2 years old. The radiograph shows an ill-defined sclerotic lesion in medial metaphyseal region of proximal right tibia (arrow). MRI shows the lesion in the metaphyseal region of proximal tibia with extension into the epiphysis and cortical destruction (arrow). Biopsy was subsequently performed and confirmed retinoblastoma metastasis.

Conclusion

Retinoblastoma is the most common intra-ocular malignancy in children. Being familiar with the MRI features indicating advanced disease is important for pediatric radiologists for accurately staging the disease and guide the clinical team for subsequent management.

Reference

1. Fabian ID, Sagoo MS. Understanding retinoblastoma: epidemiology and genetics. Community Eye Health. 2018;31(101):7. PMID: 29915458; PMCID: PMC5998389.
2. Rauschecker AM, Patel CV, Yeom KW, Eisenhut CA, Gawande RS, O'Brien JM, Ebrahimi KB, Daldrup-Link HE. High-resolution MR imaging of the orbit in patients with retinoblastoma. Radiographics. 2012 Sep-Oct;32(5):1307-26. doi: 10.1148/rg.325115176. PMID: 22977020.
3. Ancona-Lezama D, Dalvin LA, Shields CL. Modern treatment of retinoblastoma: A 2020 review. Indian J Ophthalmol. 2020 Nov;68(11):2356-2365. doi: 10.4103/ijo.IJO_721_20. PMID: 33120616; PMCID: PMC7774148.
4. TNMB: The updated TNM classification for retinoblastoma. Community Eye Health. 2018;31(101):34. PMID: 29915471; PMCID: PMC5998398.
5. Fabian ID, Reddy A, Sagoo MS. Classification and staging of retinoblastoma. Community Eye Health. 2018;31(101):11-13. PMID: 29915461; PMCID: PMC5998397.

Comparison of Abdominal Ultrasonography and Radiography for Predicting Surgical Intervention in Necrotizing Enterocolitis: A Meta-analysis

A Difadyaputra[1], RC Putri[2]

[1] *Faculty of Medicine, Pembangunan Nasional "Veteran" Jakarta University, Indonesia*
[2] *Faculty of Medicine, Udayana University, Indonesia*

Comparison of Abdominal Ultrasonography and Radiography for Predicting Surgical Intervention in Necrotizing Enterocolitis: A Meta-analysis

A. Difadyaputra [1] R.C.Putri [2]
Faculty of Medicine, Pembangunan Nasional "Veteran" Jakarta University . Faculty of Medicine, Udayana University

Background

Necrotizing enterocolitis (NEC) is a severe digestive condition that mostly impacts premature infants, leading to significant morbidity and mortality. Abdominal ultrasonography (AUS) is being used more frequently in combination with traditional abdominal radiography (AXR) to identify NEC and predicts its outcomes. However, there is a lack of studies evaluating the findings on both modalities to predict the need for surgery or mortality outcomes in NEC.

Purpose

To compare the findings of AUS and AXR in predicting the need for surgical intervention or mortality in NEC patients.

Methods

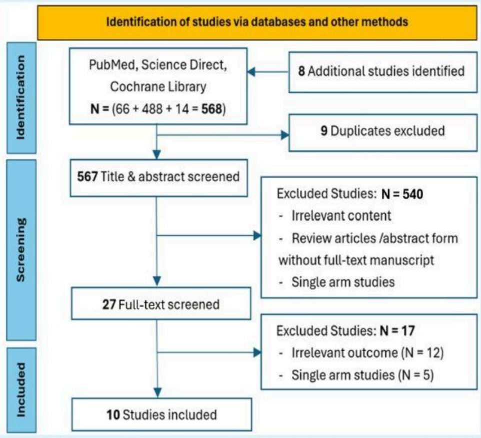

Inclusion Criteria

- Studies comparing AUS and AXR findings and and their association with surgical management or mortality outcomes in NEC.

Exclusion Criteria

- Abstract form without full-text manuscript, single-arm studies, case reports, review articles, languages other than English.
- Article/data cannot be accessed or extracted

Keywords

"(Necrotizing enterocolitis) AND (Ultrasonography OR sonography OR ultrasound) AND (abdominal x-ray OR abdominal radiograph OR abdominal radiography OR x-ray OR KUB)"

Outcomes

Surgery or death

Database

PubMed, Science Direct, and Cochrane Library

Results and Discussion

Study	Selection	Comparability	Outcome	Total Score	Quality
Muchantef et al, 2013	****	*	***	8	Good
Garbi-Goutel et al, 2013	****	*	***	8	Good
Staryszak et.al, 2015	***-	-	***	6	Fair
Prithviraj et. Al, 2015	****	-	***	7	Good
He et al, 2016	****	-	***	7	Good
Wang et al, 2016	****	*	***	8	Good
Lazow et al, 2021	****	*	***	8	Good
Chen et al, 2018	****	-	***	7	Good
Saad et al, 2018	****	*	***	8	Good
Yu et al, 2022	****	*	***	8	Good

Ultrasonography findings	Studies (N)	Patients (N)	Odds Ratio	95% CI	p-value
Pneumatosis Intestinalis	10	262	2.36	1.45 – 3.83	0.0005*
Pneumoperitoneum	6	63	10.09	2.38 – 42.83	0.002*
Portal Venous Gas	8	140	2.29	1.08 – 4.87	0.03*
Echogenicity	3	56	2.61	1.17 – 5.80	0.02*
Bowel Wall Thickening	10	309	4.29	3.11 – 5.92	<0.00001*
Bowel Wall Thinning	7	63	3.91	1.30 – 11.76	0.02*
Absent/reduced peristaltic	7	257	7.37	2.99 – 18.16	<0.0001*
Focal Fluid Collection	7	108	5.88	1.96 – 17.66	0.002*
Simple Ascites	5	133	1.44	0.24 – 8.69	0.69
Complex Ascites	3	44	12.10	4.69 – 31.25	<0.00001*
Dilated Bowel	4	84	5.14	0.88 – 29.90	0.07
Increased Perfusion	4	82	4.75	1.24 – 18.17	0.02*

*A correlation was considered significant if $p<0.05$, N = Number

Radiography findings	Studies (N)	Patients (N)	Odds Ratio	95% CI	p-value
Pneumatosis Intestinalis	9	381	2.34	1.23 – 4.46	0.009*
Pneumoperitoneum	8	58	13.35	4.15 – 42.92	<0.0001*
Portal Venous Gas	8	76	5.14	2.66 – 9.94	<0.00001*
Gasless Abdomen	3	101	1.07	0.42 – 2.71	0.89
Dilated Bowel	7	279	1.79	0.93 – 3.44	0.08
Bowel Wall Thickening	3	150	1.39	0.24 – 8.09	0.71

*A correlation was considered significant if $p<0.05$, N = Number

Imaging Modalities	Findings	Medical / No surgical group		Surgical or Death Group		OR	p-value
		Patients (T=688)	%	Patients (T=285)	%		
AUS	Pneumatosis	156	22.6	106	37.2	2.36	0.0005*
	Pneumoperitoneum	83	12	50	17.5	10.09	0.002*
	Portal venous gas	129	18.75	61	21.4	2.29	0.03*
	Bowel Wall Thickening	149	21.6	160	56.1	4.29	<0.00001*
	Dilated Bowel	32	4.6	52	18.2	5.14	0.07
AXR	Pneumatosis	260	37.8	121	42.4	2.34	0.009*
	Pneumoperitoneum	6	0.87	52	18.2	13.35	<0.0001*
	Portal venous gas	32	4.65	44	15.4	5.14	<0.00001*
	Bowel Wall Thickening	104	15.1	46	16.1	1.39	0.71
	Dilated Bowel	170	24.7	109	45.2	1.79	0.08

*A correlation was considered significant if $p<0.05$, T = Total

Among the 973 infants studied, 285 (29.3%) required surgery or died. The review included seven retrospective cohort studies, two prospective cohort studies, and one case series. Gestational ages ranged from 20 to 40 weeks, with birth weights from 540 to 4410 grams. NEC was diagnosed or symptoms appeared between 2 and 60 days of age.

Strength: First meta-analysis conducted to compare imaging modalities to predict surgical intervention or death in NEC.

Limitations: Small sample size, publication bias, variability in the studies

Conclusion

Pneumoperitoneum and complex ascites on AUS were strongly associated with the need for surgery or death, whereas only pneumoperitoneum on AXR had a strong association. Most AUS findings, apart from simple ascites and bowel dilation, correlate with the need for surgery or mortality in NEC. AUS offers additional insights that AXR cannot, including detailed visualization of abdominal wall, fluid, perfusion, peristalsis, and echogenicity. Future research should explore the advantages of combining both AXR and AUS for better predicting NEC outcomes.

Reference

1. Patel RM, Kandefer S, Walsh MC, Bell EF, Carlo WA, Laptook AR, et al. Causes and Timing of Death in Extremely Premature Infants from 2000 through 2011. New England Journal of Medicine. 2015 Jan 22;372(4):331–40.
2. Zani A, Pierro A. Necrotizing enterocolitis: controversies and challenges. F1000Research. 2015 Nov 30;4:1373.
3. Kim WY, Kim WS, Kim IO, Kwon TH, Chang W, Lee EK. Sonographic evaluation of neonates with early-stage necrotizing enterocolitis. Pediatric Radiology. 2005 Aug 3;35(11):1056–61.
4. Muchantef K, Epelman M, Darge K, Kirpalani H, Laje P, Anupindi SA. Sonographic and radiographic imaging features of the neonate with necrotizing enterocolitis: correlating findings with outcomes. Pediatric Radiology. 2013 Jun 15;43(11):1444–52.
5. Garbi-Goutel A, Brévaut-Malaty V, Panuel M, Michel F, Merrot T, Gire C. Prognostic value of abdominal sonography in necrotizing enterocolitis of premature infants born before 33 weeks gestational age. Journal of Pediatric Surgery. 2014 Apr;49(4):508–13.
6. He Y, Zhong Y, Yu J, Cheng C, Wang Z, Li L. Ultrasonography and radiography findings predicted the need for surgery in patients with necrotising enterocolitis without pneumoperitoneum. Acta Paediatrica. 2016 Jan 20;105(4).
7. Yu L, Liu C, Cui Y, Xue L, Ma L. Imaging manifestations of neonatal necrotizing enterocolitis to predict timing of surgery. The Turkish Journal of Pediatrics. 2022;64(4):632.
8. Prithviraj D, Sandeep B, Suresh A, Balaraju V, Mondal S. Comparison between x-ray and abdominal ultrasound findings of necrotizing enterocolitis, its usefulness in early diagnosis, prognosis, and to assess, is this is the time to change our view of surgeon's intervention according to the Bell's criteria. International Journal of Scientific Study. 2015 July;3(4):119–30.
9. Saad YG, Seif M, Mansi YA, Hashem RH. Role of Abdominal Ultrasonography in the assessment of Neonatal Necrotising Enterocolitis. The Egyptian Journal of Radiology and Nuclear Medicine. 2018 Sep 1;49(3):755–63.
10. Lazow SP, Tracy SA, Staffa SJ, Estroff JA, Parad RB, Castro-Aragon IM, et al. Abdominal ultrasound findings contribute to a multivariable predictive risk score for surgical necrotizing enterocolitis: A pilot study. American Journal of Surgery. 2021 Nov;222(5):1034–9.

A Comparison of Automatic Bone Age Assessments between the Left and Right Hands: A Tool for Filtering Measurement Errors

Saelin Oh[1], Yeo Eun Han[1], Kyu-Chong Lee[1], Jae-Joon Lee[2], Chang Ho Kang[1], Kyung-Sik Ahn[1]

[1] Department of Radiology, Anam Hospital, Korea University College of Medicine, Republic of Korea
[2] Crescom, Seongnam, Republic of Korea

A Comparison of Automatic Bone Age Assessments between the Left and Right Hands: A Tool for Filtering Measurement Errors

Saelin Oh[1], Yeo Eun Han[1], Kyu-Chong Lee[1], Jae-Joon Lee[2], Chang Ho Kang[1] and Kyung-Sik Ahn[1]

[1] Department of Radiology, Anam Hospital, Korea University College of Medicine
[2] Crescom, Seongnam, Republic of Korea

Background

- Bone age assessment (BAA) is a clinical procedure used to evaluate skeletal maturity in pediatric patients .
- Various automatic and deep learning methods for BAA have been proposed, which have demonstrated high accuracy, reproducibility, and time efficiency.
- It is time to focus on how to use it efficiently in real practice without missing inevitable errors.

Purpose

- To introduce an upgraded automatic hand bone alignment technique and to propose right-hand BAA as a tool for filtering out measurement errors

Materials and Methods

- Our study included 757 children underwent bilateral radiography at our institution between January and December 2023.
- The digital images were processed using an automated MediAI-BA method; the model relies on hybrid TW3 and GP AI-based automatic bone age measurements.
- The absolute difference between each hand BAA by the model (ADBH model) was calculated. Bland–Altman, Passing–Bablok, and Spearman correlation coefficients were analyzed.

Results

Variables	ADBH Model ≤ 0.5 Year (n = 698)	ADBH Model > 0.5 Year (n = 59)	P
Age, years	8.77 ± 2.66	8.55 ± 2.73	0.555
Male-to-female ratio	295:403	26:33	0.788
Left-hand BAA	9.18 ± 3.21	8.78 ± 2.27	0.356
Right-hand BAA	9.22 ± 3.22	9.00 ± 3.39	0.620
ADBH model	0.198 ± 0.145 (0.187, 0.209)	0.667 ± 0.109 (0.638, 0.695)	<0.001
Developmental stage			0.025
Pre-puberty	201/698 (28.2%)	26/59 (44.1%)	0.018
Early and mid-puberty	462/698 (66.2%)	29/59 (49.2%)	0.010
Late puberty	28/698 (4.0%)	2/59 (3.4%)	1.000
Post puberty	7/698 (1.0%)	2/59 (3.4%)	0.151

Table1. A comparison of the characteristics of the study population

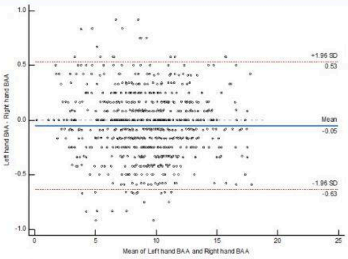

Figure1. The Bland–Altman plots indicate an agreement between each hand's bone age assessment. The dotted horizontal lines represent a standard deviation of ± 2.

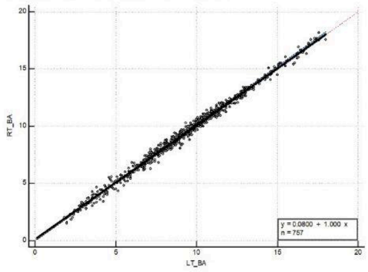

Figure2. The Passing–Bablok regression analysis showed that the overall correlation of the bone age assessment between both hands was excellent, with no significant deviation from linearity in this association (p = 0.15).

	Left Hand	Right Hand	P
Automatic bone age assessment by the model	8.78 ± 3.27	9.00 ± 3.39	0.011
Reference standard bone age reference by two reviewers	8.93 ± 3.29	8.89 ± 3.33	0.157
Mean absolute difference	0.409 ± 0.335 (0.322, 0.467)	0.424 ± 0.329 (0.339, 0.510)	0.809
Median	0.354	0.330	
Range	0–1.75	0–1.33	

Tabe2. A comparison of the bone age assessment by the model and the reference standard.

Conclusions

- Our study showed an excellent overall correlation of BAAs between both hands using the model and provided the possibility of using the right-hand BAA as a validation tool.
- Perceptible differences between each hand may indicate a large measurement error and thus may be a signal for manual supervision.